Journal of Applied Physics ARTICLE scitation.org/journal/jap

Quantitative, experimentally-validated, model of MoS_2 nanoribbon Schottky field-effect transistors from subthreshold to saturation

Cite as: J. Appl. Phys. **127**, 065705 (2020); doi: 10.1063/1.5127769
Submitted: 13 September 2019 · Accepted: 28 January 2020 ·
Published Online: 10 February 2020

View Online Export Citation CrossMark

Paolo Paletti,[1,a)] Sara Fathipour,[1] Maja Remškar,[2] and Alan Seabaugh[1,b)]

AFFILIATIONS

[1]Department of Electrical Engineering, University of Notre Dame, Notre Dame, Indiana 46556, USA
[2]Solid State Physics Department, Józef Stefan Institute, SI-1000 Ljubljana, Slovenia

[a)]**Author to whom correspondence should be addressed:** Paolo.Paletti.1@nd.edu
[b)]**Electronic mail:** Alan.C.Seabaugh.1@nd.edu

ABSTRACT

We investigate the channel length dependence of the electrical characteristics of chemical vapor transport (CVT)-grown MoS_2 nanoribbon (NR) Schottky barrier field-effect transistors to provide insights into the transport properties of such nanostructures. The MoS_2 NRs form spontaneously during the CVT growth, without the application of etching. Back gated transmission line measurement FETs were fabricated on a 45 μm-long NR with channel lengths ranging between 200 nm and 3 μm. Contact and sheet resistances were extracted from the electrical measurements and their back-gate bias dependence was analyzed. Numerical modeling based on a virtual probe approach combined with the Landauer formalism shows excellent agreement with the measurements. The model enables a quantitative extraction of the intrinsic FET properties, e.g., mean-free-path and electron mobility, and their dependence on carrier density and investigation of plausible trap distributions. A record electron mobility for a MoS_2 NR channel of $\sim$81 $cm^2/V\,s$ was achieved.

I. INTRODUCTION

Two-dimensional (2D) transition metal dichalcogenides (TMDs), such as MoS_2, have been widely explored for electronic applications as potential Si channel material replacement in field-effect transistors (FETs).[1,2] Ultra thin body thickness with atomic-layer control and the absence of surface dangling bonds are key enablers to preserve electrostatic gate control at ultrashort channel lengths, and the relatively larger electron effective mass along the transport direction with respect to Si allows for a reduction of direct source-to-drain leakage currents in the FET's OFF-state and, thus, a diminished drain-induced barrier lowering effect.[3–7]

While big strides have been accomplished in the synthesis and wafer-level processing of TMD-based planar sheets,[8] TMD materials such as MoS_2, and WS_2 have also been grown in nanoribbon (NR) and nanotube (NT) forms.[9–13] These TMD nanostructures have been predominantly achieved by either sulfurization of tungsten or molybdenum films,[9,10] or by chemical vapor transport (CVT) techniques.[11–14] Synthesized NRs and NTs are intriguing from a transistor point of view since no etching step is required to define the channel area, thus preserving the transport properties of the pristine films, in contrast to FETs built using top-down approaches.[15–21] Density functional theory simulations predict a strain-induced reduction of the MoS_2 NT energy gap when diameters are reduced to $\sim$10 nm,[22] which makes NTs attractive for tunnel FET applications. It has also been shown theoretically that lateral confinement, at the limits of width scaling, in MoS_2 NRs results in the appearance of localized edge states within the MoS_2 gap,[23,24] which could enable a new class of *cold source* steep-slope devices.[25]

Only a few reports have been published investigating carrier transport in synthesized TMD NRs[26–29] or NTs.[28–35] Best published MoS_2 NR FET results indicate electron mobility, μ_n, as high as 36 $cm^2/V\,s$, with an I_{ON}/I_{OFF} ratio $> 10^3$ (NR width, $W = 321$ nm, and thickness, $t = 12$ nm).[28] For comparisons, Kotekar-Patil[20] *et al.* reported I_{ON}/I_{OFF} ratios $\sim 10^5$, μ_n up to 50 $cm^2/V\,s$, and $I_{ON} \sim 38\,\mu A/\mu m$ ($V_{DS} = 2$ V) for a lithographically-defined 50 nm-wide, 500 nm-long monolayer MoS_2 NR FET. With the aid of an ion doping technique, contact resistance as low as $0.75\,k\Omega/\mu m$ and ON-currents, $I_{ON} \sim 230\,\mu A/\mu m$ ($V_{DS} = 1.2\,V$) were obtained,[26] as well as reconfigurable unipolar *n*- and *p*-type, and simultaneous *pn* doping for the same MoS_2 NR channel ($W = 700\,nm$ and $t = 13\,nm$).[27]

In this paper, through the analysis of FETs of variable channel lengths fabricated on a single MoS_2 NR, we demonstrate in Sec. II record electron mobilities equal to $81\,cm^2/V\,s$ and improved I_{ON} at comparable drain bias with respect to best prior reports. An analytical FET model able to couple Schottky barrier (SB)-limited carrier injection at the semiconductor/metal interface together with scattering-limited transport across the 2D channel is presented in Sec. III, and applied to fit experimental data in Sec. IV. We consider for the first time whether it is possible to quantitatively describe the measured transport properties of MoS_2 FETs from subthreshold to saturation.

II. DEVICE FABRICATION AND ELECTRICAL CHARACTERIZATIONS

MoS_2 NRs were grown by CVT inside an evacuated silica ampoule, starting from an MoS_2 powder using an iodine transport agent.[36] The ampoule was sealed at a pressure $\sim 7 \times 10^{-4}$ Pa and placed in a two-zone furnace where the hot and cold sides of the oven were kept at 1133 and 1010 K, respectively, with a temperature gradient of ~6.2 K/cm. CVT growth lasted 21 days after which the silica ampoule was slowly cooled to room temperature at a controlled rate of 60 °C/h. The slow growth rate from the vapor phase during lasting chemical transport reactions results in the simultaneous growth of different types of MoS_2 nanostructures, such as NRs, NTs, as well as thin flakes. Low defect density MoS_2 NRs with thickness in the range of ~10 nm, length up to several hundreds of micrometers and homogenous width is typically found. However, precise size-control using the described CVT growth methods cannot be achieved due to the nature of their nucleation process. In fact, NR growth starts from the collapse of a NT when it meets an obstacle in the growth process. When collapsed, such a tube continues to grow in length. Due to the chirality of the NTs, strain in the lattice of the NRs causes twisting along the longitudinal axis. Synthesis, material characterization, and nucleation processes have been previously discussed by Remškar.[12,13]

A NR with a total length of $45\,\mu m$ was chosen for device fabrication. A false-colored scanning electron micrograph (SEM) image of the transmission line measurement (TLM) structure characterized in this study is shown Fig. 1(a), and a zoomed in SEM image of the NR top part is presented in Fig. 1(b). The complete process flow consisted of electron beam evaporation, in order, of Ti/Au (5 nm/100 nm) for the back-gate (BG) contact on the back of a p^+ Si wafer, atomic-layer deposition of 27 nm of Al_2O_3, and tape transfer of the MoS_2 NR. A TLM structure was patterned using electron beam lithography, followed by electron beam evaporation of Ti/Au (5 nm/100 nm) metal contacts. The schematic cross section of the fabricated devices with complete annotations of the

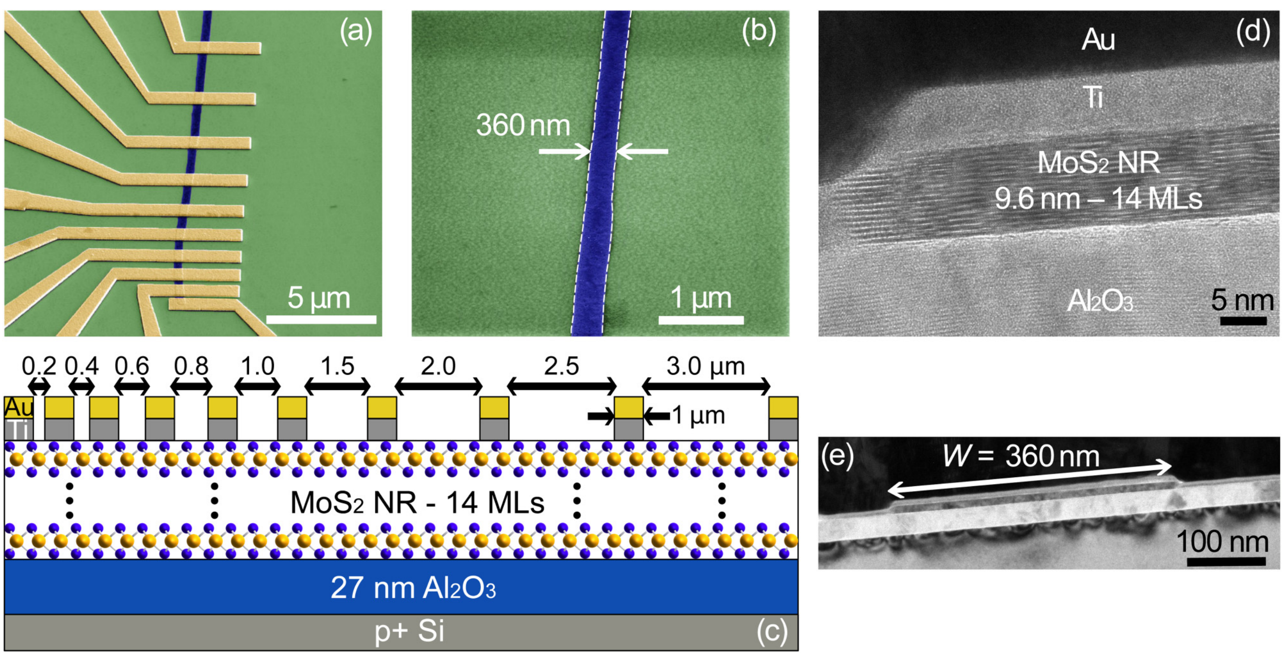

FIG. 1. (a) False-colored SEM top view of the fabricated TLM devices. The Al_2O_3 BG is colored in green, the MoS_2 NR is in blue, and the Ti/Au metal leads are in orange. Contact length is $1\,\mu m$, and the NR measures $\sim 45\,\mu m$. (b) Zoom-in of the NR top part. Dashed white lines follow the NR edges. (c) Schematic cross section of the TLM structure. Nine FETs were fabricated from a single NR. Channel lengths range from 200 nm up to $3\,\mu m$. (d) High magnification TEM cross section. (e) Low magnification TEM cross section.

different FET channel lengths, ranging from 3 μm down to 200 nm is shown in Fig. 1(c). Transmission electron micrograph (TEM) cross sections were taken following the electrical measurements to establish the channel geometry. The NR has a thickness of ~9.6 nm, corresponding to 14 MoS_2 layers, Fig. 1(d), and measures 360 nm in width, Fig. 1(e).

Drain current vs BG voltage, I_D–V_{BG}, transfer characteristics for a drain bias $V_{DS} = 0.5$ V of five selected FETs are shown in Fig. 2(a). For $L = 200$ nm, $I_{ON}/I_{OFF} > 2 \times 10^4$, $I_{ON} = 18.7\,\mu$A/μm at $V_{BG} = 3$ V, with minimum subthreshold swing SS = 0.46 V/dec. The ON-state drain current reduces to 12.9 μA/μm at $L = 2\,\mu$m, and SS = 0.47 V/dec. The less than proportional drain current reduction as a function of channel length is a consequence of both the variations of threshold voltage, V_T, among the different devices, i.e., different overdrive voltages at $V_{BG} = 3$ V, and the influence of the Schottky contacts. The same characterization is plotted in Fig. 2(b) in a linear scale to enhance the V_T differences. The threshold voltage is obtained with a linear extrapolation for each channel length as indicated by the dotted lines in Fig. 2(b);

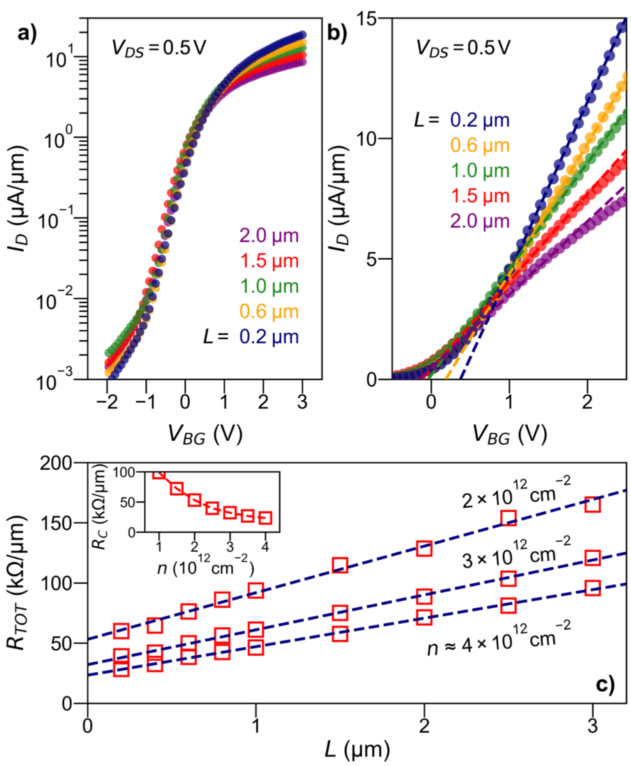

FIG. 2. (a) Semilogarithmic plot of the transfer characteristics, I_D vs V_{BG}, for five FETs with channel lengths ranging from 200 nm to 3 μm. (b) I_D–V_{BG} curves in a linear scale. Dashed lines indicate a linear fit of the characteristics above the threshold for $V_{GS} - V_T > V_{DS}$. The threshold voltage, V_T is estimated from the abscissa intercept. (c) R_{TOT} (red squares) as a function of channel length, L, calculated for different electron densities, n. Linear scaling with respect to L is indicated by blue dashed lines. Inset: contact resistance, R_C, as a function of carrier density.

V_T ranges between 0.375 V and −0.152 V for $L = 200$ nm and $L = 2\,\mu$m, respectively, which is attributed to different impurity/oxide charge distributions at the FETs' TMD/BG interfaces.

To account for the V_T variations, the total resistance, $R_{TOT} = V_{DS}/I_D$, vs L is plotted in Fig. 2(c), for various sheet electron densities, n. Assuming a linear dependence of n with respect to the BG voltage above threshold, $n \approx C_{OX}(V_{BG} - V_T)/q$, where $C_{OX} = 0.26\,\mu F/cm^2$ is the BG oxide capacitance density for a 27 nm-thick Al_2O_3, and q is the electron charge. The dashed lines in Fig. 2(c) represent a simple linear scaling of R_{TOT} with respect to L, which indicates a good agreement with the experimental results upon the corrections for the V_T shifts. This represents an indirect evidence of uniform transport properties and charge injection through the contacts at the same carrier density. The ordinate intercept yields the total contact resistance per unit width, R_C, and its dependence with respect to the carrier density is plotted in the inset of Fig. 2(c). Contact resistance decreases from 99 to 23 kΩ/μm for n ranging from 1×10^{12} to 4×10^{12} cm^{-2}, respectively, as the BG modulates the injection through the SB at the contacts. For a Schottky FET, R_C is dominated by the source contact at low V_{DS}. In Fig. 2(c), the slope of the least-square fitting corresponds to the sheet resistance, R_{SH}, in units of kΩ/, which is related to the effective mobility, $\mu_{EF} = (qnR_{SH})^{-1}$. For a carrier concentration $n = 2 \times 10^{12}$ cm^{-2}, $\mu_{EF} = 81$ cm^2/V s. The TLM analysis permits an accurate estimate of μ_{EF} since it allows decoupling the contributions of R_{SH} and R_C due to the Schottky contacts from R_{TOT}. Table I summarizes measurements on MoS_2 NR FETs. Compared to previously published synthesized[28] as well as top-down defined[20] MoS_2 NR best results, this measurement shows significantly higher electron mobility than the 50 cm^2/V s reported by Kotekar-Patil, Table I.

III. 2D FET WITH GATED SB CONTACTS

A semianalytical model based on the virtual probe approach[37–39] is employed to describe 2D FETs with SB contacts. A sketch of the equivalent circuit used to model the 2D channel FET with Schottky contacts is shown in Fig. 3. The potential at the center of the ballistic SB FETs and the TMD FET sandwiched in between is imposed by the vertical electrostatics, with the gate terminal of each transistor tied together. The head and tail SB FETs are connected to the source (S) and drain (D) reservoirs through SB contacts, while the inner TMD FET is connected to two, fully thermalizing Büttiker probes, with Fermi potential $\mu_1 = -qV_1$, and $\mu_2 = -qV_2$. The voltages V_1 and V_2 are obtained by imposing current continuity across the three series transistors. The directions of the diode symbols in Fig. 3 indicate that the S (D) SB are in reverse (forward) bias if a positive V_{DS} is applied at the terminals. Our model assumes for simplicity an ideal 2D channel. This approximation is reasonable when the channel thickness is smaller than the depletion width.

A. Intrinsic 2D FET in linear region

In the case of near-equilibrium transport in the channel, an average Fermi potential $E_F = (E_{FS} + E_{FD})/2$, is defined with E_{FS} and E_{FD} representing the source and drain Fermi potentials,

TABLE I. MoS_2 nanoribbon FETs prior reports.

μ_n (cm^2/V s)	I_{ON} (μA/μm)	I_{ON}/I_{OFF}	W (nm)	t_{NR} (nm)	Oxide	MoS_2
21.8[a]	16.4	$>10^4$	60	6	SiO_2	Bulk
36–50[b]	40	$>10^5$	50	1 ML	SiO_2	Bulk
36	0.8	$>10^3$	140	7	Al_2O_3	CVT
81	18.7	$>2\times10^4$	360	9.6	Al_2O_3	CVT
L_{CH} (nm)	t_{OX} (nm)	V_{DS} (V)	V_{GS} (V)	Author		Reference
1000	300	2	50	Liu		16
500	300	1	60	Kotekar-Patil		20
3000	26	0.3	1	Fathipour		28
200	27	0.5	3	This work		

[a] $W = 2\,\mu$m.
[b] $V_{DS} = 0.1$–0.6 V.

respectively. Thus, the 2D electron sheet carrier density, n is equal to

$$n = k_B T D_0 \ln\left[1 + e^{(E_F - E_C)/k_B T}\right], \tag{1}$$

where k_B is Boltzmann constant, T is temperature, $D_0 = g_S g_V m^*/2\pi\hbar^2$ is the 2D density of state, g_S and g_V are the spin and valley degeneracies, respectively, $\hbar$ is the reduced Planck constant, and E_C is the conduction band edge. To account for nonidealities in the vertical electrostatics, we consider acceptorlike traps, i.e., negatively charged when ionized,[40] each represented by a delta function in energy, characterized by an effective trap density D_{IT}, and located at an energy E_{IT} below the conduction band,[41] such that the total density of ionized traps, N_{IT}, can be expressed as

$$N_{IT} = \sum_i \frac{D_{IT,i}}{1 + \exp[(E_C - E_F + E_{IT,i})/k_B T]}. \tag{2}$$

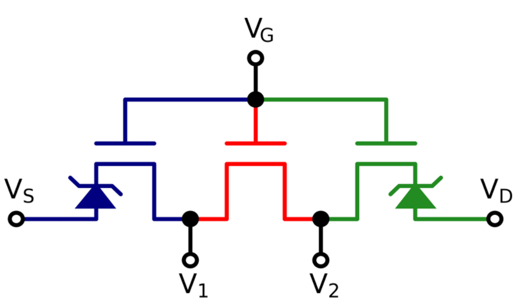

FIG. 3. Equivalent circuit of the 2D FET with Schottky contacts. The S and D transistors are modeled as ballistic SB FETs with a Schottky contact connected to the external reservoirs, V_S and V_D, respectively, and an ohmic contact connected to an internal virtual probe. The intrinsic TMD FET is fully connected by the two Büttiker probes, V_1 and V_2. All the transistor gates are tied to the same gate voltage, V_G.

The sum of the total mobile charges, interface traps, and constant donor impurities, N_D, must be equal to the charge induced by the electrostatic coupling to the gate,

$$q^2 \frac{(n + N_{IT} - N_D)}{C_{OX}} + (E_F - E_C) = q(V_{BG} - V_{FB}), \tag{3}$$

where V_{FB} is the flatband voltage. Equation (3) can be solved iteratively to map E_C as a function of E_F and V_{BG}.

The drain current, I_D, is computed using the Landauer–Büttiker formalism,[42,43]

$$I_D = \frac{2q}{h}\int_{E_C}^{\infty} M(E)T(E)[f(E_{FS}) - f(E_{FD})]\mathrm{d}E. \tag{4}$$

In Eq. (4), $M(E) = 2g_V W\sqrt{2m^*(E - E_C)}/h$ is the number of modes, h is Planck's constant, m^* is the electron effective mass, $T(E)$ is the channel transmission, $f(E_{FS})$ and $f(E_{FD})$ are the source and drain Fermi-Dirac distributions, respectively. We define the channel transmission,[44]

$$T(E) = \frac{\lambda(E)}{\lambda(E) + L}, \tag{5}$$

where $\lambda(E)$ is the energy-dependent mean-free-path (MFP) for backscattering and L is the channel length. We assume power-law relationships between energy and MFP, and consider charged-impurity (CI) and phonon (PH) scattering as the dominant scattering mechanisms,[45]

$$\lambda_{CI}(E) = \frac{\lambda_{CI0}}{N_{IT}}\left(\frac{E - E_C}{k_B T}\right)^{3/2}, \tag{6}$$

$$\lambda_{PH}(E) = \lambda_{PH0}\left(\frac{E - E_C}{k_B T}\right)^{1/2}, \tag{7}$$

where λ_{CI0} and λ_{PH0} are fitting parameters associated with the corresponding scattering processes. The two energy-dependent MFPs are then combined together using Matthiessen's rule,

$$\frac{1}{\lambda(E)} = \frac{1}{\lambda_{CI}(E)} + \frac{1}{\lambda_{PH}(E)}. \quad (8)$$

B. Channel FET in far-from-equilibrium operation

In far-from-equilibrium conditions, the Fermi level can no longer be assumed constant along the channel, therefore a position-dependent quasi-Fermi level $E_{Fn}(x)$ is defined. Equations (1) and (2) need to be rewritten by substituting $E_F \rightarrow E_{Fn}$, while in Eq. (3) qV_{BG} is replaced with $qV_{BG,CH} = qV_{BG} + E_{Fn} - E_{FS}$.[46] The charge balance equation in its nonequilibrium form reads

$$q^2 \frac{(n + N_{IT} - N_D)}{C_{OX}} + (E_{Fn} - E_C) = q(V_{BG} - V_{FB}) + E_{Fn} - E_{FS}. \quad (9)$$

The drain current is written from the Pao–Sah formulation,[47]

$$I_D = \frac{qW\mu}{L} \int_{V_S}^{V_D} n \, dV. \quad (10)$$

Following the derivation of Marin *et al.*,[46] an expression of $(E_{Fn} - E_C)$ in terms of n is obtained from Eq. (1),

$$E_{Fn} - E_C = k_B T \ln\left(e^{n/N_C} - 1\right), \quad (11)$$

where $N_C = k_B T D_0$ is the conduction band effective density of states, and substituted back in Eqs. (2) and (3) to obtain

$$\frac{q^2}{C_{OX}} \left[n + \sum_i \frac{D_{IT,i}\left(e^{n/N_C} - 1\right)}{e^{n/N_C} - 1 + e^{E_{IT,i}/k_B T}} \right] + k_B T \ln\left(e^{n/N_C} - 1\right)$$
$$= q\left(V_{BG} - V_{FB} + \frac{qN_D}{C_{OX}}\right) + E_{Fn} - E_{FS}. \quad (12)$$

Differentiating Eq. (12) with respect to n makes possible the change of variable $dV = -dE_{Fn}/q \rightarrow dn$ in Eq. (10),

$$I_D = \frac{q^2 W\mu}{L} \int_{n_D}^{n_S} \Big[\frac{1}{C_{OX}} + \sum_i \frac{D_{IT,i}\, e^{E_{IT,i}/k_B T} e^{n/N_C}}{C_{OX} N_C \left(e^{n/N_C} - 1 + e^{E_{IT,i}/k_B T}\right)^2}$$
$$+ \frac{k_B T e^{n/N_C}}{q^2 N_C \left(e^{n/N_C} - 1\right)} \Big] n \, dn. \quad (13)$$

Equation (13) is analytically integrable and its closed form can be written as

$$I_D = \frac{q^2 W\mu}{L} \Bigg\{ \frac{n^2}{2C_{OX}} + \frac{k_B T}{q^2} \left(N_C \mathrm{Li}_2(e^{n/N_C}) + n \ln(e^{n/N_C} - 1)\right)$$
$$+ \frac{1}{C_{OX}} \sum_i \frac{D_{IT,i}}{\left(1 - e^{-E_{IT,i}/k_B T}\right)} \Bigg[\frac{n}{e^{n/N_C} - 1 + e^{E_{IT,i}/k_B T}}$$
$$- N_C \ln\left(e^{n/N_C} - 1 + e^{E_{IT,i}/k_B T}\right) \Bigg] \Bigg\}_{n_D}^{n_S}, \quad (14)$$

where Li_2 denotes the polylogarithm function of second order, and the limits of the integrals are the electron densities n_S (n_D) at the source (drain) ends, calculated from Eq. (12) by posing $E_{Fn} = E_{FS}(E_{FD})$.

C. Ballistic SB FET

Transport in a SB FET is given by the sum of thermionic carrier injection over the thermal barrier with tunneling of charge carriers through the SB. To provide an analytical expression of the tunneling through the SB, we consider a triangular potential barrier of width Λ,

$$\Lambda = \sqrt{\frac{\varepsilon_{S,x}}{\varepsilon_{OX}} t_S \, t_{OX}}, \quad (15)$$

where $\varepsilon_{S,x}$ is the in-plane semiconductor dielectric constant, ε_{OX} is the BG oxide dielectric constant, t_S is the semiconductor body thickness, and t_{OX} is the BG oxide thickness. Considering only the lowest lying subband within the effective mass approximation, the transmission coefficient is obtained *via* the Wentzel–Kramers–Brilluoin (WKB) approximation,

$$T_{WKB}(E) = \begin{cases} 1, & E \geq \Phi_N \\ \exp\left(-\frac{8\pi}{3h}\sqrt{2m^*(\Phi_N - E)^3}\frac{\Lambda}{\Phi_N - E_C}\right), & E < \Phi_N. \end{cases} \quad (16)$$

In the above equation, Φ_N is the effective thermal barrier for electrons, and E_C is controlled by both the BG voltage and charge injection across the SB. Given a SB height for electrons, Φ_{SB}, we can define a flatband voltage at which $E_C = \Phi_{SB}$. Two different cases need to be considered. For $V_{BG} \leq V_{FB}$, only thermionic injection takes places above a thermal barrier of height, $\Phi_N = E_C$. Above flatband, $E_C < \Phi_{SB}$, $\Phi_N = \Phi_{SB}$ and the tunneling component is added.

As shown in Fig. 3, the ballistic SB FET at the S end presents a SB contact at its relative source side, and ohmic contact at the drain side (and vice versa for the ballistic SB FET at the D end). The SB is modeled as a mesoscopic scatterer for carriers entering the channel;[37,48] hence, the overall mobile charge, n, is given by the sum of forward- and backward-going fluxes,

$$n = \int_{E_C}^{\infty} \frac{D_0}{2} \left[T_{WKB} f(E_{FS}) + (2 - T_{WKB}) f(E_{FD})\right] dE. \quad (17)$$

Consistent with the ballistic approach, the trap occupation probability in Eq. (2) is computed by defining an equivalent Fermi level, E_{Feq}, given by[49]

$$\exp\left(\frac{-E_{Feq}}{k_B T}\right) = \frac{n_S}{n} \exp\left(\frac{-E_{FS}}{k_B T}\right) + \frac{n_D}{n} \exp\left(\frac{-E_{FD}}{k_B T}\right), \quad (18)$$

where n is the total electron density, and n_S (n_D) is the the electron density injected from the source (drain) computed in Eq. (17). The drain current is obtained from the Landauer–Büttiker equation,

$$I_D = \frac{2q}{h} \int_{E_C}^{\infty} M(E) T_{WKB}(E) [f(E_{FS}) - f(E_{FD})] dE. \quad (19)$$

IV. RESULTS AND DISCUSSION

To properly capture the device electrostatics, a double Gaussian D_{IT} distribution is utilized as shown in Fig. 4(a). This distribution is qualitatively similar to the energetic trap distribution extracted by Takenaka *et al.*[50] from multifrequency *C-V* measurements of MoS_2 MOS capacitors. Takenaka postulated that these defect traps might originate from sulfur vacancies. From an electrostatics point-of-view, these localized states are equivalent to an additional capacitance in parallel to the semiconductor capacitance.[40] Other physical parameters used in the simulations are the electron SB, $\Phi_{SB} = 0.2\,\text{eV}$, $m^*/m_0 = 0.5$, with m_0 being the electron rest mass, $g_S = 2$ and $g_V = 6$. The effective mass of 0.5 is a reasonable estimate for the multilayer MoS_2 based on the tight-binding simulations of Zahid *et al.*[51] The device characteristic length $\Lambda = 19.7\,\text{nm}$, hence for simplicity the TMD FET channel length is approximated with $L_{CH} = L - 2\Lambda$.

At low V_{DS}, we assume that the channel FET is in near-equilibrium conditions in order to reveal the intrinsic transport properties of the NR channels. Figure 4(b) shows the position of the Fermi level with respect to the CB edge as a function of V_{BG}. Due to the presence of a D_{IT} distribution centered at $\sim$370 mV below E_C, E_F is pinned for a negative V_{BG}, while for a large positive V_{BG} degenerate conditions are met. For $V_{BG} = 3\,\text{V}$, the electron density reads $n = 3.5 \times 10^{12}\,\text{cm}^{-2}$ [Fig. 4(c)]. The ionized trap density vs. V_{BG} is reported in Fig. 4(d) indicating an increased in N_{IT} from 2.0×10^{12} to $8.2 \times 10^{12}\,\text{cm}^{-2}$, by sweeping V_{BG} from -2 to 3 V, respectively. The interplay between charged interface traps and mobile carriers in the vertical electrostatics is summarized in Fig. 4(e); when the Fermi level is deep into the bandgap, i.e., in the subthreshold regime, the interface trap capacitance, C_{IT}, dominates the quantum capacitance, C_Q. However, for a large V_{BG}, E_F approaches E_C, and $C_Q \gg C_{IT}$. The interface trap capacitance is estimated from the SS of the measured FETs using the relationship $\text{SS} = (k_B T/q)\ln(10)[1 + C_{IT}/C_{OX}]$. Combined with Fig. 4(a) which maps V_{BG} onto E_F, it is possible to compare the results of the extraction, open circles in Fig. 4(e), with the modeled results, showing excellent agreement. Closer to the band edge, the extracted C_{IT} follows the trend imposed by C_Q as expected. Since the total channel capacitance, given by the sum of C_{IT} and C_Q, is voltage dependent, this results in a voltage drop partition between the semiconductor channel, V_{CH}, and the oxide insulator, V_{OX}, as a function of *n*, as shown in Fig. 4(f).

The simulated transfer characteristics are plotted in Fig. 4(g) for all the fabricated FETs. The only free parameter allowed for the fitting is a relative threshold voltage shift to be consistent with Figs. 1(a) and 1(b). To be able to see all the transfer curves and the model fits within the same graph, a spacing of 1 V is set between each of the I_D–V_{BG} characteristics. The modeling results are in excellent agreement with experiments, from deep subthreshold to accumulation. The greatest deviation is found for the 200 nm-long FET. For this case, the ON-state current is still in reasonable agreement with the measurements, suggesting uniform SB height and

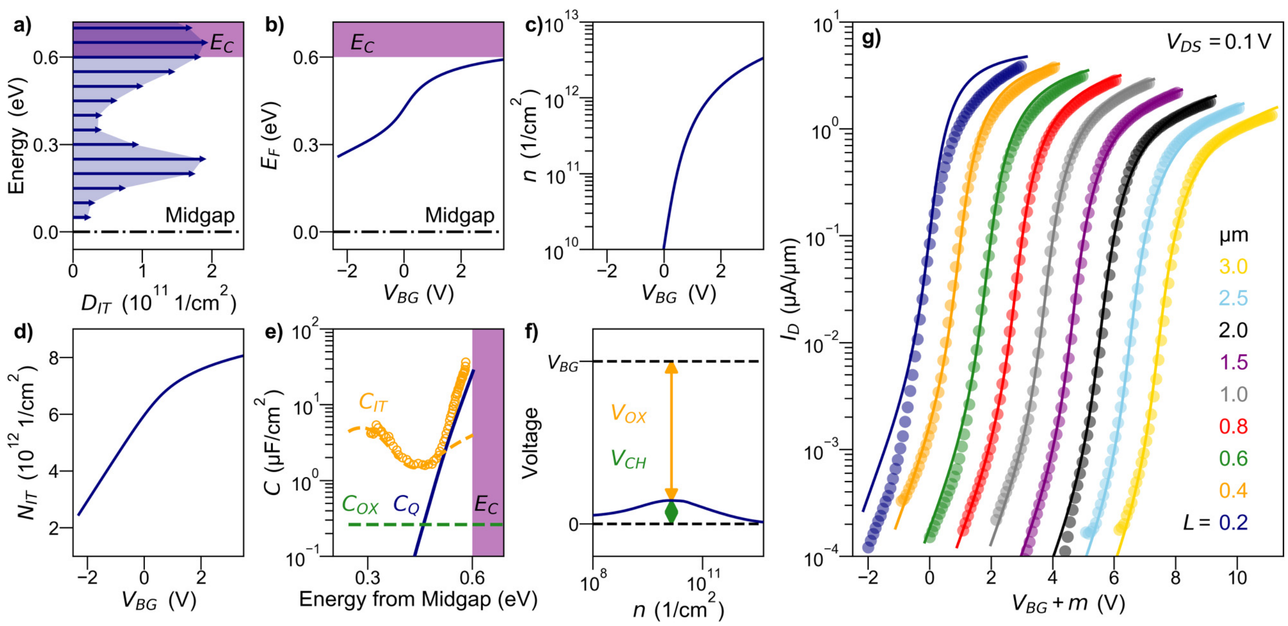

FIG. 4. (a) Distribution of interface acceptor traps, D_{IT}, employed in the simulations consisting of a train of δ functions following double Gaussian distributions. Simulation results [(b)–(f)] for the intrinsic 2D FET with $L = 3\,\mu\text{m}$. (b) Fermi level, E_F, (c) sheet electron density *n*, and (d) ionized trap density, N_{IT}, vs back-gate voltage, V_{BG}. (e) Capacitance densities vs E_F: interface trap, C_{IT}, channel quantum, C_Q, and oxide, C_{OX}. Open circles represent C_{IT} as extracted from the measured FET subthreshold slope. (f) Proportion of V_{OX} and V_{CH} to the applied V_{BG} as a function of *n*. (g) Measured vs simulated transfer characteristics for all the TLM FETs. Each trace is shifted by *m* V to allow comparison, where from left to right, $m = 0, 1, 2, \ldots, 8$.

channel scattering. Refinement in the D_{IT} distribution could improve the agreement for this particular FET, but D_{IT} shown in Fig. 4(a) provides a good accounting of the measured characteristics over the full set of devices.

With this understanding, a quantitative analysis of the NR transport properties is enabled by the Landauer formalism.[44] For a small V_{DS}, Eq. (4) can be rewritten in the following form:

$$I_D = \left[\frac{2q^2}{h}\int T(E)\,M(E)\left(-\frac{\partial f_0}{\partial E}\right)\mathrm{d}E\right]V, \tag{20}$$

where the term enclosed by square brackets is the channel conductance, $G = \sigma_{2D}W/L$, and σ_{2D} is the 2D conductivity. Under diffusive transport conditions, $T(E) \approx \lambda(E)/L$, and by indicating the number of modes per channel width as $M_{2D}(E) = M(E)/W$, we obtain an equation for σ_{2D} independent of the device geometry,

$$\sigma_{2D} = \frac{2q^2}{h}\int \lambda(E)\,M_{2D}(E)\left(-\frac{\partial f_0}{\partial E}\right)\mathrm{d}E. \tag{21}$$

Following the treatment of Lundstrom and Jeong,[44] the number of modes in the Fermi window, $\langle M_{2D}(E)\rangle$, and the average mean-free-path for backscattering, $\langle\langle\lambda(E)\rangle\rangle$, are equal to

$$\langle M_{2D}(E)\rangle = \int M_{2D}(E)\left(-\frac{\partial f_0}{\partial E}\right)\mathrm{d}E$$
$$\langle\langle\lambda(E)\rangle\rangle = \frac{\int \lambda(E)\,M_{2D}(E)\left(-\frac{\partial f_0}{\partial E}\right)\mathrm{d}E}{\int M_{2D}(E)\left(-\frac{\partial f_0}{\partial E}\right)\mathrm{d}E}. \tag{22}$$

Substituting the above results back into Eq. (21), σ_{2D} becomes

$$\sigma_{2D} = \frac{2q^2}{h}\,\langle\langle\lambda(E)\rangle\rangle\,\langle M_{2D}(E)\rangle = q\mu_n n. \tag{23}$$

From Eq. (23), the scattering-limited mobility written in the Landauer form is equal to

$$\mu_n = \frac{2q}{nh}\int \lambda(E)\,M_{2D}(E)\left(-\frac{\partial f_0}{\partial E}\right)\mathrm{d}E, \tag{24}$$

which is valid in the diffusive limit.

The average MFP vs electron density is plotted in Fig. 5. The MFP tops at 5.5 nm, for $n = 2\times10^{7}\,\mathrm{cm}^{-2}$, and then degrades at a larger n due to an increased density of ionized acceptorlike traps increasing charged impurity scattering. The minimum MFP reads 4.5 nm, for $n = 1.9\times10^{12}\,\mathrm{cm}^{-2}$. The fitting parameters used in the power-law relationships of Eqs. (6) and (7) are equal to $\lambda_{CI0} = 0.65\,\mathrm{nm}^{-1}$, and $\lambda_{PH0} = 10\,\mathrm{nm}$. Figure 5 shows also the computed μ_n using Eq. (24). The electron mobility is $102\,\mathrm{cm}^2/\mathrm{V\,s}$ at low carrier densities and reaches $83\,\mathrm{cm}^2/\mathrm{V\,s}$ for $n = 2\times10^{12}\,\mathrm{cm}^{-2}$, which is in good agreement with the TLM extraction. A plot of the 2D conductivity vs $(E_F - E_C)$ is shown in the inset.

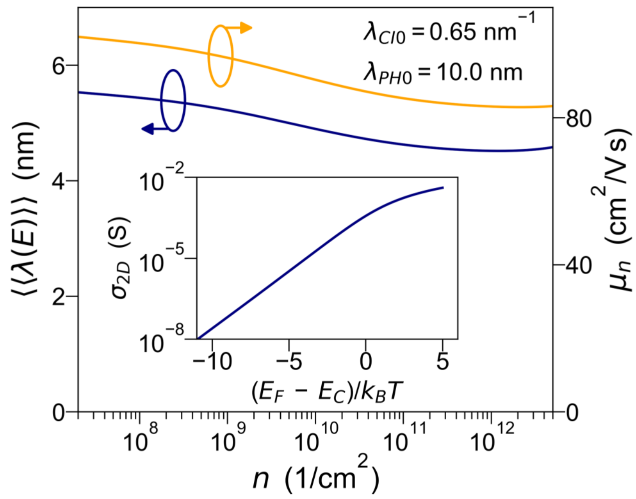

FIG. 5. Transport parameters extracted from the Landauer formalism. Average MFP, $\langle\langle\lambda(E)\rangle\rangle$, and electron mobility, μ_n, vs carrier density n. Inset: 2D conductivity, σ_{2D}, as a function of the normalized energy difference, $(E_F - E_C)/k_BT$.

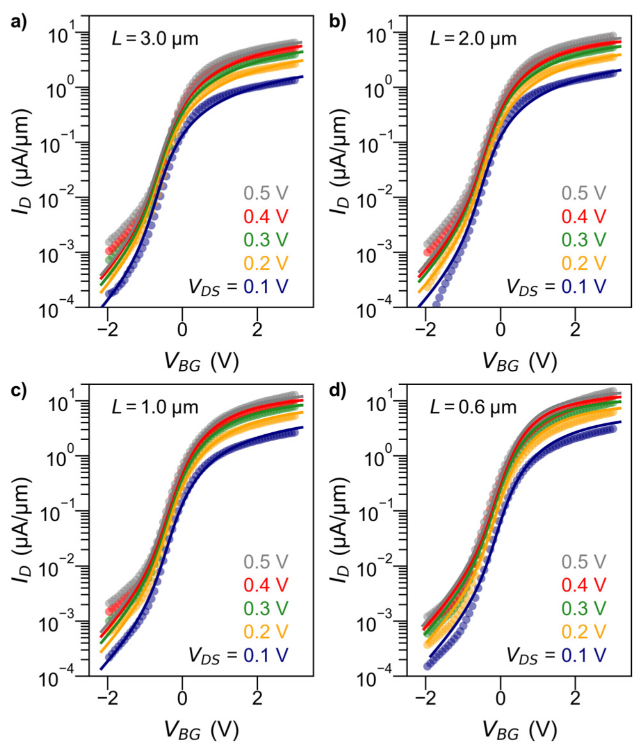

FIG. 6. Measured vs simulated I_D–V_{BG} characteristics taken at different V_{DS}. FET channel lengths are (a) $3\,\mu$m, (b) $2\,\mu$m, (c) $1\,\mu$m, and (d) $0.6\,\mu$m, respectively.

While the near-equilibrium picture provides physical insights regarding the main scattering mechanisms in play and is able to derive transport properties such as MFP and carrier mobility as a function of carrier density, it is applicable when the voltage drop across the channel FET is on the order of $k_B T/q$. The drift-diffusion model can then be utilized to capture the drain voltage dispersion by employing the mobility results stemming from the Landauer analysis. With the same set of physical parameters, the I_D–V_{BG} measurements are fitted substituting with the drift-diffusion FET model described in Sec. III B, using a constant carrier mobility, $\mu_n = 85\,\text{cm}^2/\text{V s}$. Since mobility is a function of carrier density, we consider an averaged value obtained within the carrier density range, $10^{10} \leq n \leq 5 \times 10^{12}\,\text{cm}^{-2}$, which covers the near and superthreshold regime of interest. The results of the computation are shown in Fig. 6 for four devices of channel lengths equal to (a) $3\,\mu$m, (b) $2\,\mu$m, (c) $1\,\mu$m, and (d) $0.6\,\mu$m, respectively.

The comparison with the measured transfer characteristics indicates a good agreement from weak subthreshold to accumulation in the ON-state, for all the applied drain-to-source biases. Deep in the OFF-state, the differences between the simulations and the experiments are more accentuated as a consequence of device-to-device variations in the trap distributions. As already mentioned in Fig. 4(e), in deep subthreshold the electrostatic coupling of the channel potential with the gate is dictated by the series combination of C_{OX} with C_{IT} ($\gg C_Q$), therefore a variation in the D_{IT} greatly impacts the slope of the I_D–V_{BG} characteristics. The model agreement with experiments from subthreshold to saturation is notable despite the use of a field-independent mobility.

V. CONCLUSION

Electrical measurements of MoS_2 FETs with variation in channel length were used to validate numerical large-signal models of the FET transport. Our semianalytical model based on the virtual probe approach was shown to be in excellent agreement with measurements from subthreshold to saturation and was utilized to extract intrinsic transport properties. The dominant scattering mechanisms were identified, as well as the dependence on carrier densities of MFP and electron mobility. A drift-diffusion model was also derived that captures the V_{DS} dependence of the BG transfer characteristics. The electron mobility of $81\,\text{cm}^2/\text{V s}$ was obtained, for which MoS_2 NRs is the highest reported.

ACKNOWLEDGMENTS

The authors would like to thank Tatyana Orlova and Sergei Rouvimov at the Notre Dame Integrated Imaging Facility for TEM specimen preparation and imaging.

REFERENCES

[1] G. Fiori, F. Bonaccorso, G. Iannaccone, T. Palacios, D. Neumaier, A. Seabaugh, S. K. Banerjee, and L. Colombo, "Electronics based on two-dimensional materials," Nat. Nanotechnol. **9**, 768 (2014).
[2] S. S. Sylvia, K. Alam, and R. K. Lake, "Uniform benchmarking of low-voltage van der Waals FETs," IEEE J. Exploratory Solid State Comput. Devices Circuits **2**, 28–35 (2016).
[3] L. Liu, Y. Lu, and J. Guo, "On monolayer MoS_2 field-effect transistors at the scaling limit," IEEE Trans. Electron Devices **60**, 4133–4139 (2013).
[4] Y. Yoon, K. Ganapathi, and S. Salahuddin, "How good can monolayer MoS_2 transistors be?,' Nano Lett. **11**, 3768–3773 (2011).
[5] C. D. English, K. K. Smithe, R. L. Xu, and E. Pop, "Approaching ballistic transport in monolayer MoS_2 transistors with self-aligned 10 nm top gates," in *2016 IEEE International Electron Devices Meeting (IEDM)* (IEEE, 2016), pp. 5–6.
[6] A. Nourbakhsh, A. Zubair, R. N. Sajjad, A. Tavakkoli K. G., W. Chen, S. Fang, X. Ling, J. Kong, M. S. Dresselhaus, E. Kaxiras, K. K. Berggren, D. Antoniadis, and T. Palacios, "MoS_2 field-effect transistor with sub-10 nm channel length," Nano Lett. **16**, 7798–7806 (2016).
[7] S. B. Desai, S. R. Madhvapathy, A. B. Sachid, J. P. Llinas, Q. Wang, G. H. Ahn, G. Pitner, M. J. Kim, J. Bokor, C. Hu, H.-S. P. Wong, and A. Javey, "MoS_2 transistors with 1-nanometer gate lengths," Science **354**, 99–102 (2016).
[8] N. Briggs, S. Subramanian, Z. Lin, X. Li, X. Zhang, K. Zhang, K. Xiao, D. Geohegan, R. Wallace, L.-Q. Chen, M. Terrones, A. Ebrahimi, S. Das, J. Redwing, C. Hinkle, K. Momeni, A. van Duin, V. Crespi, S. Kar, and J. A. Robinson, "A roadmap for electronic grade 2D materials," 2D Mater. **6**, 022001 (2019).
[9] R. Tenne, L. Margulis, M. Genut, and G. Hodes, "Polyhedral and cylindrical structures of tungsten disulphide," Nature **360**, 444 (1992).
[10] Y. Feldman, E. Wasserman, D. J. Srolovitz, and R. Tenne, "High-rate, gas-phase growth of MoS_2 nested inorganic fullerenes and nanotubes," Science **267**, 222–225 (1995).
[11] M. Remškar, A. Mrzel, Z. Skraba, A. Jesih, M. Ceh, J. Demšar, P. Stadelmann, F. Lévy, and D. Mihailovic, "Self-assembly of subnanometer-diameter single-wall MoS_2 nanotubes," Science **292**, 479–481 (2001).
[12] M. Remškar, Z. Skraba, F. Cleton, R. Sanjines, and F. Levy, "MoS_2 as microtubes," Appl. Phys. Lett. **69**, 351–353 (1996).
[13] M. Remškar, Z. Škraba, M. Regula, C. Ballif, R. Sanjinés, and F. Levy, "New crystal structures of WS_2: Microtubes, ribbons, and ropes," Adv. Mater. **10**, 246–249 (1998).
[14] R. Nitsche, "The growth of single crystals of binary and ternary chalcogenides by chemical transport reactions," J. Phys. Chem. Solids **17**, 163–165 (1960).
[15] F. Zhang, C.-H. Lee, J. A. Robinson, and J. Appenzeller, "Exploration of channel width scaling and edge states in transition metal dichalcogenides," Nano Res. **11**, 1768–1774 (2018).
[16] H. Liu, J. Gu, and P. D. Ye, "MoS_2 nanoribbon transistors: Transition from depletion mode to enhancement mode by channel-width trimming," IEEE Electron Device Lett. **33**, 1273–1275 (2012).
[17] D. S. Fox, Y. Zhou, P. Maguire, A. O'Neill, C. Ó'Coileáin, R. Gatensby, A. M. Glushenkov, T. Tao, G. S. Duesberg, I. V. Shvets, M. Abid, M. Abid, H.-C. Wu, Y. Chen, J. N. Coleman, J. F. Donegan, and H. Zhang, "Nanopatterning and electrical tuning of MoS_2 layers with a subnanometer helium ion beam," Nano Lett. **15**, 5307–5313 (2015).
[18] X. Liu, T. Xu, X. Wu, Z. Zhang, J. Yu, H. Qiu, J.-H. Hong, C.-H. Jin, J.-X. Li, X.-R. Wang, L.-T. Sun, and W. Guo, "Top-down fabrication of sub-nanometre semiconducting nanoribbons derived from molybdenum disulfide sheets," Nat. Commun. **4**, 1776 (2013).
[19] J.-B. Wu, H. Zhao, Y. Li, D. Ohlberg, W. Shi, W. Wu, H. Wang, and P.-H. Tan, "Monolayer molybdenum disulfide nanoribbons with high optical anisotropy," Adv. Opt. Mater. **4**, 756–762 (2016).
[20] D. Kotekar-Patil, J. Deng, S. Wong, C. S. Lau, and K. E. J. Goh, "Single layer MoS_2 nanoribbon field effect transistor," Appl. Phys. Lett. **114**, 013508 (2019).
[21] S. Chen, S. Kim, W. Chen, J. Yuan, R. Bashir, J. Lou, A. M. van der Zande, and W. P. King, "Monolayer MoS_2 nanoribbon transistors fabricated by scanning probe lithography," Nano Lett. **19**, 2092–2098 (2019).
[22] G. Seifert, H. Terrones, M. Terrones, G. Jungnickel, and T. Frauenheim, "Structure and electronic properties of MoS_2 nanotubes," Phys. Rev. Lett. **85**, 146 (2000).
[23] H. Pan and Y.-W. Zhang, "Edge-dependent structural, electronic and magnetic properties of MoS_2 nanoribbons," J. Mater. Chem. **22**, 7280–7290 (2012).
[24] Q. Yue, S. Chang, J. Kang, X. Zhang, Z. Shao, S. Qin, and J. Li, "Bandgap tuning in armchair MoS_2 nanoribbon," J. Phys. Condens. Matter **24**, 335501 (2012).

[25]D. Logoteta, M. G. Pala, J. Choukroun, P. Dollfus, and G. Iannaccone, "A steep-slope MoS_2-nanoribbon MOSFET based on an intrinsic cold-contact effect," IEEE Electron Device Lett. **PP**(99), 1 (2019).
[26]S. Fathipour, H.-M. Li, M. Remškar, L. Yeh, W. Tsai, Y. Lin, S. Fullerton-Shirey, and A. Seabaugh, "Record high current density and low contact resistance in MoS_2 FETs by ion doping," in *2016 International Symposium on VLSI Technology, Systems and Application (VLSI-TSA)* (IEEE, 2016), pp. 1–2.
[27]C. Alessandri, S. Fathipour, H. Li, I. Kwak, A. Kummel, M. Remškar, and A. C. Seabaugh, "Reconfigurable electric double layer doping in an MoS_2 nanoribbon transistor," IEEE Trans. Electron Devices **64**, 5217–5222 (2017).
[28]S. Fathipour, M. Remškar, A. Varlec, A. Ajoy, R. Yan, S. Vishwanath, S. Rouvimov, W. Hwang, H. Xing, D. Jena, and A. Seabaugh, "Synthesized multi-wall MoS_2 nanotube and nanoribbon field-effect transistors," Appl. Phys. Lett. **106**, 022114 (2015).
[29]S. Fathipour, H. Li, P. Paletti, M. Remškar, S. Fullerton-Shirey, and A. Seabaugh, "First synthesized WS_2 nanotube and nanoribbon field effect transistors grown by chemical vapor transport," in *2017 75th Annual Device Research Conference (DRC)* (IEEE, 2017), pp. 1–2.
[30]H. E. Unalan, Y. Yang, Y. Zhang, P. Hiralal, D. Kuo, S. Dalal, T. Butler, S. N. Cha, J. E. Jang, K. Chremmou, G. Lentaris, D. Wei, R. Rosentsveig, K. Suzuki, H. Matsumoto, M. Minagawa, Y. Hayashi, M. Chhowalla, A. Tanioka, W. I. Milne, R. Tenne, and G. A. J. Amaratunga, "ZnO nanowire and WS_2 nanotube electronics," IEEE Trans. Electron Devices **55**, 2988–3000 (2008).
[31]M. Remškar, A. Mrzel, M. Virsek, M. Godec, M. Krause, A. Kolitsch, A. Singh, and A. Seabaugh, "The MoS_2 nanotubes with defect-controlled electric properties," Nanoscale Res. Lett. **6**, 26 (2011).
[32]M. Strojnik, A. Kovic, A. Mrzel, J. Buh, J. Strle, and D. Mihailovic, "MoS_2 nanotube field effect transistors," AIP Adv. **4**, 097114 (2014).
[33]M. Sugahara, H. Kawai, Y. Yomogida, Y. Maniwa, S. Okada, and K. Yanagi, "Ambipolar transistors based on random networks of WS_2 nanotubes," Appl. Phys. Express **9**, 075001 (2016).
[34]H. Kawai, M. Sugahara, R. Okada, Y. Maniwa, Y. Yomogida, and K. Yanagi, "Thermoelectric properties of WS_2 nanotube networks," Appl. Phys. Express **10**, 015001 (2016).
[35]R. Levi, O. Bitton, G. Leitus, R. Tenne, and E. Joselevich, "Field-effect transistors based on WS_2 nanotubes with high current-carrying capacity," Nano Lett. **13**, 3736–3741 (2013).
[36]M. Remškar, Z. Škraba, F. Cleton, R. Sanjines, and F. Levy, "MoS_2 microtubes: An electron microscopy study," Surf. Rev. Lett. **5**, 423–426 (1998).
[37]P. Michetti and G. Iannaccone, "Analytical model of one-dimensional carbon-based Schottky-barrier transistors," IEEE Trans. Electron Devices **57**, 1616–1625 (2010).
[38]M. Büttiker, "Small normal-metal loop coupled to an electron reservoir," Phys. Rev. B **32**, 1846 (1985).
[39]M. Buttiker, "Role of quantum coherence in series resistors," Phys. Rev. B **33**, 3020 (1986).
[40]E. H. Nicollian and J. R. Brews, *MOS (Metal Oxide Semiconductor) Physics and Technology* (Wiley, New York, 1982), pp. 192, 195.
[41]S. V. Suryavanshi and E. Pop, "S2DS: Physics-based compact model for circuit simulation of two-dimensional semiconductor devices including non-idealities," J. Appl. Phys. **120**, 224503 (2016).
[42]R. Landauer, "Spatial variation of currents and fields due to localized scatterers in metallic conduction (and comment)," J. Math. Phys. **37**, 5259–5268 (1996).
[43]S. Datta, *Electronic Transport in Mesoscopic Systems* (Cambridge University Press, 1997), p. 110.
[44]M. Lundstrom and C. Jeong, *Near-Equilibrium Transport: Fundamentals and Applications* (World Scientific Publishing Company, 2012), Vol. 2.
[45]I. S. Esqueda, H. Tian, X. Yan, and H. Wang, "Transport properties and device prospects of ultrathin black phosphorus on hexagonal boron nitride," IEEE Trans. Electron Devices **64**, 5163–5171 (2017).
[46]E. G. Marin, S. J. Bader, and D. Jena, "A new holistic model of 2-D semiconductor FETs," IEEE Trans. Electron Devices **65**, 1239–1245 (2018).
[47]H. C. Pao and C.-T. Sah, "Effects of diffusion current on characteristics of metal-oxide (insulator)-semiconductor transistors," Solid State Electron. **9**, 927–937 (1966).
[48]A. Hazeghi, T. Krishnamohan, and H.-S. P. Wong, "Schottky-barrier carbon nanotube field-effect transistor modeling," IEEE Trans. Electron Devices **54**, 439–445 (2007).
[49]M. Visciarelli, A. Gnudi, E. Gnani, and S. Reggiani, "A full-quantum simulation study of InGaAs NW MOSFETs including interface traps," in *2016 46th European Solid-State Device Research Conference (ESSDERC)* (IEEE, 2016), pp. 180–183.
[50]M. Takenaka, Y. Ozawa, J. Han, and S. Takagi, "Quantitative evaluation of energy distribution of interface trap density at MoS_2 MOS interfaces by the Terman method," in *2016 IEEE International Electron Devices Meeting (IEDM)* (IEEE, 2016), pp. 5–8.
[51]F. Zahid, L. Liu, Y. Zhu, J. Wang, and H. Guo, "A generic tight-binding model for monolayer, bilayer and bulk MoS_2," AIP Adv. **3**, 052111 (2013).